Nuclear Inst. and Methods in Physics Research, A 916 (2019) 169–178

Contents lists available at ScienceDirect

Nuclear Inst. and Methods in Physics Research, A

journal homepage: www.elsevier.com/locate/nima

A space-resolved extreme ultraviolet spectrometer for radial profile measurement of tungsten ions in the Experimental Advanced Superconducting Tokamak

Ling Zhang [a,*], Shigeru Morita [b,c], Zhenwei Wu [a], Zong Xu [d,e], Xiuda Yang [a,f], Yunxin Cheng [a,f], Qing Zang [a], Haiqing Liu [a], Yong Liu [a], Hongming Zhang [a], Tetsutarou Ohishi [b,c], Yingjie Chen [a], Liqing Xu [a], Chengrui Wu [a,f], Yanmin Duan [a], Wei Gao [a], Juan Huang [a], Xianzu Gong [a], Liqun Hu [a]

[a] Institute of Plasma Physics Chinese Academy of Sciences, Hefei 230026, Anhui, China
[b] National Institute for Fusion Science, Toki 509-5292, Gifu, Japan
[c] Department of Fusion Science, Graduate University for Advanced Studies, Toki 509-5292, Gifu, Japan
[d] Advanced Energy Research Center, Shenzhen University, Shenzhen 518060, China
[e] Key Laboratory of Optoelectronic Devices and Systems of Ministry of Education and Guangdong Province, College of Optoelectronic Engineering, Shenzhen University, Shenzhen 518060, China
[f] Science Island Branch of Graduate School, University of Science and Technology of China, Hefei 230026, China

ARTICLE INFO

Keywords:
EAST tokamak
EUV spectrometer
Tungsten spectrum
Tungsten ion density

ABSTRACT

In order to study the radial transport of tungsten ions in long-pulse H-mode discharges, a space-resolved spectrometer working at 30–520 Å has been newly developed to measure a radial profile of the tungsten line emission. The spectrometer is installed behind a long extension vacuum tube connected to a horizontal midplane diagnostic port of EAST tokamak. The long distance between the plasma and spectrometer, 8835.5 mm, enables observation of the radial profile of impurity line emissions in a wide vertical range of $-8.5 \leq Z \leq 40$ cm ($-0.1 \leq \rho \leq 0.6$). A good spectral resolution of $\Delta\lambda_0 = 4 - 5$ pixels at the foot position of spectral line profiles and a high spatial resolution of $\Delta Z = 2.5$ cm are obtained in addition to a sufficient temporal resolution, e.g. 50 ms/frame. As a result, accurate radial profiles have been successfully obtained in EAST Ohmic and H-mode discharges for several impurity species such as carbon, oxygen, argon, iron and tungsten. The radial profiles of tungsten line emissions from $W^{42+} - W^{45+}$ ions with 4p–4s transitions measured at two wavelength ranges of 45–70 Å and 120–140 Å are analyzed for the ion density evaluation based on the photon emissivity coefficient from ADAS database. The result shows that the density of $W^{43+} - W^{45+}$ ions ranges at 2–6 $\times 10^8$ cm^{-3} in steady H-mode discharges with $T_e(0) = 3$ keV and $n_e(0) = 4 \times 10^{13}$ cm^{-3}.

1. Introduction

Impurities play an important role for maintaining high-performance plasmas in magnetic confinement fusion research because the radiation power loss and bulk ion dilution caused by the impurity ions easily degrade the plasma performance. It is well known the radiation loss quickly increases with atomic number of the impurity element. In ITER [1], on the other hand, tungsten is used as the divertor material instead of carbon. The use of tungsten is also planned in CFETR [2]. In order to examine an effect of the tungsten divertor on tokamak discharges, several tokamak devices have installed tungsten plasma facing components (PFCs), e.g. ASDEX-U [3] and WEST [4] with full tungsten environment, JET with ITER-like wall [5] and EAST with tungsten monoblock upper divertor [6]. To explore the compatibility of such high-Z PFCs to the plasma performance, two tile rings with W-coated TZM (Titanium–Zirconium–Molybdenum) alloy inserts have been installed on graphite tiles in the lower divertor of DIII-D [7] and tungsten-coated tiles have been installed at the outboard side of the lower divertor of JT-60U [8]. To study the tungsten spectra and tungsten transport, the tungsten is also externally introduced into the plasma with different techniques, e.g. tungsten pellet injection in LHD [9,10], tungsten laser blow-off in HL-2A [11] and Alcator C-Mod [12] and tungsten particle dropper in NSTX [13].

Passive spectroscopy is a unique tool for studying detailed behavior of the tungsten ions in fusion plasmas including the temporal evolution and spatial distribution. Spectral lines from impurity ions measured with passive spectroscopy are emitted in different wavelength ranges such as visible, vacuum ultraviolet (VUV), extreme ultraviolet (EUV) and X-ray, and the wavelength range for tungsten spectroscopy varies with the

* Corresponding author.
E-mail addresses: zhangling@ipp.ac.cn (L. Zhang), zwwu@ipp.ac.cn (Z. Wu).

https://doi.org/10.1016/j.nima.2018.11.082
Received 19 September 2018; Received in revised form 15 November 2018; Accepted 15 November 2018
Available online 23 November 2018
0168-9002/

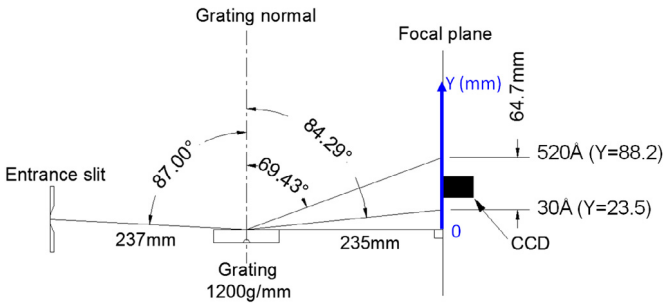

Fig. 1. Top view of optical layout of space-resolved EUV spectrometer.

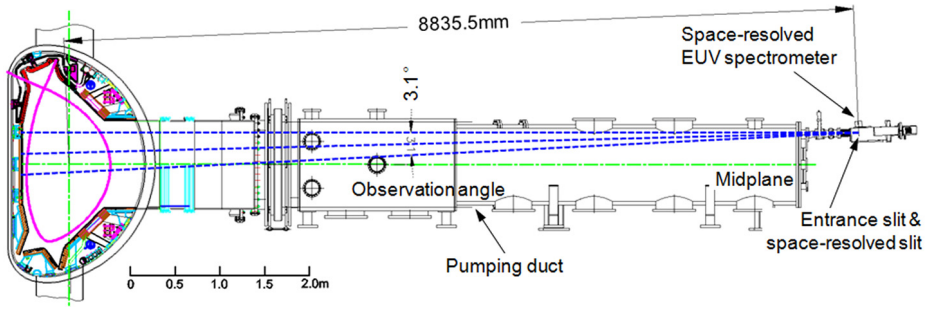

Fig. 2. Side view of space-resolved EUV spectrometer installed on EAST. The angle of declination is $\theta_{EUV} = 1.4°$ at the central viewing axis. The viewing area of the spectrometer is 48.5 cm in the vertical direction and 12.0 cm in the horizontal direction at the plasma center.

ionization stage of tungsten ions to be studied. For instance, a visible W I line at 4009 Å has been widely used to evaluate the tungsten flux at the divertor target [3,14,15]. Spectral lines from W^{3+}–W^{6+} and W^{19+}–W^{45+} ions have been observed at VUV range of 500–1500 Å [16] and EUV range of 10–500 Å [9,13,17–21], respectively. X-ray lines are generally used at 4–8 Å for tungsten ions in higher ionization stages such as W^{39+}–W^{49+} [18,22]. Since the central electron temperature of ITER plasmas is extremely high, e.g. $T_{e0} \sim 15$–20 keV, VUV, EUV and X-ray spectroscopy can be applied to the scrape-off layer (SOL), edge and core plasmas [20], respectively.

Recently, grazing-incidence flat-field EUV spectrometers with a laminar-type concave holographic grating with varied-line-spacing (VLS) groove and a back-illuminated charge-coupled device (CCD) have been developed in several fusion devices to observe the tungsten spectra because of the good spectral resolution, high throughput and weak contribution of higher order light. EUV spectrometers called "EUV_Long" and "EUV_Short" working at 50–500 Å and 10–130 Å have been developed in LHD [9,23], respectively. Similar grazing-incidence EUV spectrometers have been also developed in ASDEX-U [17,24] and NSTX tokamaks [25]. In EUV spectroscopy, the radial profile measurement of impurity line emissions is also possible, if a space-resolved slit is installed at an entrance slit. Space-resolved EUV spectrometers called "EUV_Long2" and "EUV_Short2" working at 60–400 Å [26] and 10–130 Å [27] have been developed in LHD to study impurity transport [28]. A new method on the absolute intensity calibration of the EUV spectrometers has been attempted in LHD based on the bremsstrahlung continuum measurement. An excellent result on the absolute calibration is obtained over a wider wavelength range [29,30,27]. As a result, an accurate quantitative analysis becomes possible on the tungsten density evaluation [14]. Tungsten EUV spectroscopy with good temporal and spatial resolutions is applied to the identification of pseudo-continuum spectra called unresolved transition arrays (UTA) for the diagnostics of tungsten ions in edge plasmas of ITER [20]. Similar space-resolved EUV spectrometers have been installed on HL-2A [31] and EAST [32,33]. An EUV spectrometer for two-dimensional distribution measurement has also been developed in LHD for impurity transport study in stochastic magnetic field layer [34,35].

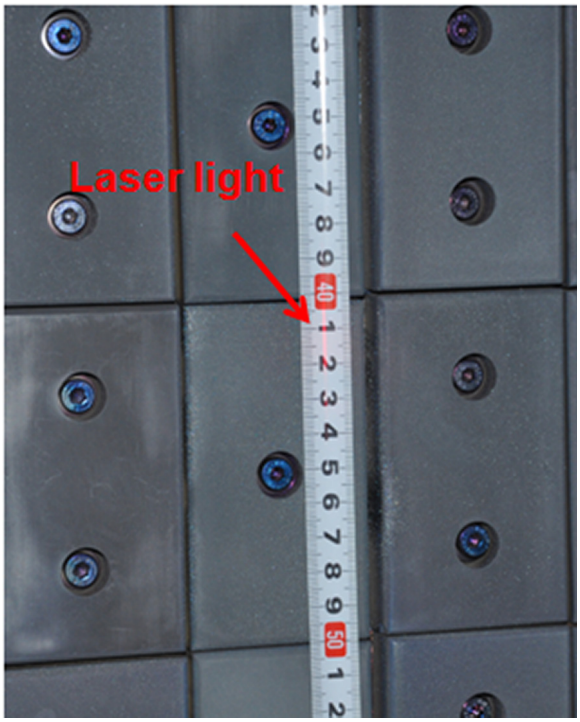

Fig. 3. Positional calibration in vacuum vessel of EAST for checking optical axis of space-resolved EUV spectrometer using laser which is attached to the spectrometer for alignment. The vertical red line indicated with 'Laser light' shows central optical axis of the space-resolved spectrometer.

The EAST tokamak has been equipped with an upper tungsten divertor since 2014 to improve the heat exhaust capability and to examine the ITER-like divertor configuration [6]. To study the tungsten transport in EAST discharges, tungsten spectra have been measured with

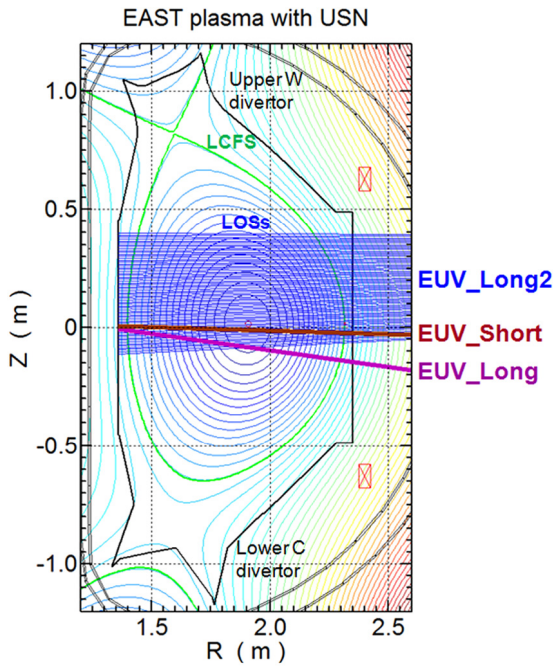

Fig. 4. Lines of sight (LOS) of space-resolved EUV spectrometer (EUV_Long2: blue thin lines) and fast-response EUV spectrometers (EUV_Short: brown thick line and EUV_Long: purple thick line).

fast-time-response EUV spectrometers working in wavelength ranges of 10–130 Å (EUV_Short) and 20–500 Å (EUV_Long) [36] at time resolution of 5 ms. Recently, on the other hand, a space-resolved EUV spectrometer working in 30–520 Å (EUV_Long2) has been developed to measure the radial profile of tungsten line emissions in long-pulse H-mode discharges with high heating power.

In this paper, characteristics and performance of the space-resolved EUV spectrometer are described in Section 2. Tungsten spectra observed in radiofrequency (RF)-heated H-mode discharges combined with lower hybrid wave (LHW) current driving and heating, ion cyclotron range of heating (ICRF) and electron cyclotron heating (ECH) are shown in Section 3. Radial profiles of tungsten line emissions are presented in Section 4 with a preliminary result on the tungsten ion density evaluation. Finally, the paper is summarized in Section 5.

2. Space-resolved EUV spectrometer

2.1. Arrangement of EUV spectrometer for spatial measurement

In the EUV spectrometer developed in the present study a flat-field focus along the direction of wavelength dispersion, which enables the use of a linear detector such as CCD, is achieved by a laminar VLS concave holographic grating (Shimadzu 3–002) used at an angle of incidence of 87° as shown in Fig. 1. A back-illuminated CCD (Andor DO920-BN) with sensitive area of 26.6 × 6.6 mm^2 and pixel numbers of 1024 × 255 (26 × 26 μm^2/pixel) is adopted for recording the two-dimensional image. The long axis of the CCD is set perpendicular to the horizontal wavelength dispersion for the radial profile measurement along the vertical direction, while the short axis of the CCD is set along the horizontal wavelength dispersion for the spectrum measurement. A wide entrance slit of 100 μm width is used to obtain sufficient signal intensity in the profile measurement. Meanwhile, a relatively narrow spatial resolution slit with vertical opening width of 1 mm is used to obtain a good spatial resolution. A stepping motor installed on the spectrometer makes it possible to move the CCD along the wavelength dispersion on the focal plane for the selection of wavelength range to be measured. A software program is also developed to remotely control the stepping motor.

The distance from the entrance slit to the grating center is 237 mm, and the distance from grating center to the focal plane is 235 mm, as shown in Fig. 1. The EUV light from EAST plasmas passing through the entrance slit is diffracted by the grating and focused on the flat focal plane according to the following equation of

$$m\lambda = \delta_0 (\sin\alpha + \sin\beta), \quad (1)$$

where m, λ, δ_0, α and β mean the diffraction order, the wavelength of spectral line, the grating groove spacing (1200/mm at grating center) and the angles of incidence and diffraction. The angle of diffraction can be changed in the range of $-84.29° \le \beta \le -69.43°$. Since the CCD size along the wavelength dispersion is small, i.e. 6.6 mm, a movable double stage system is adopted to the space-resolved EUV spectrometer to move the CCD over a wider range. As a result, a wide wavelength range of 30–520 Å is observable by moving the CCD in the range of 64.7 mm.

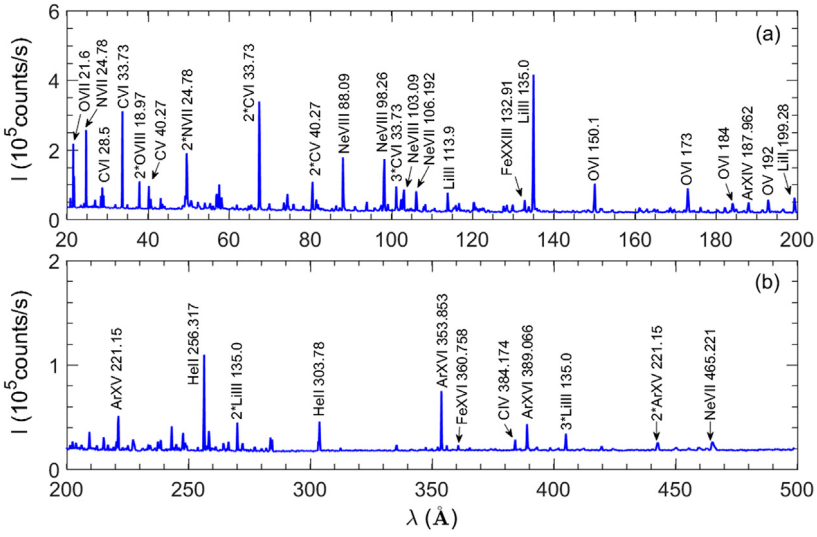

Fig. 5. Typical EUV spectra observed with fast-response EUV spectrometers in EAST Ohmic discharges (T_{e0} = 1 keV) at wavelength ranges of (a) 20–200 Å and (b) 200–500 Å. The spectrum at 20–40 Å is measured with EUV_Short in a single discharge. The spectrum at 40–500 Å measured with EUV_Long using three discharges are superposed by three spectra at different wavelength ranges. Ne and Ar are observed as an aftereffect of the radiative divertor experiment with Ne and Ar seeding.

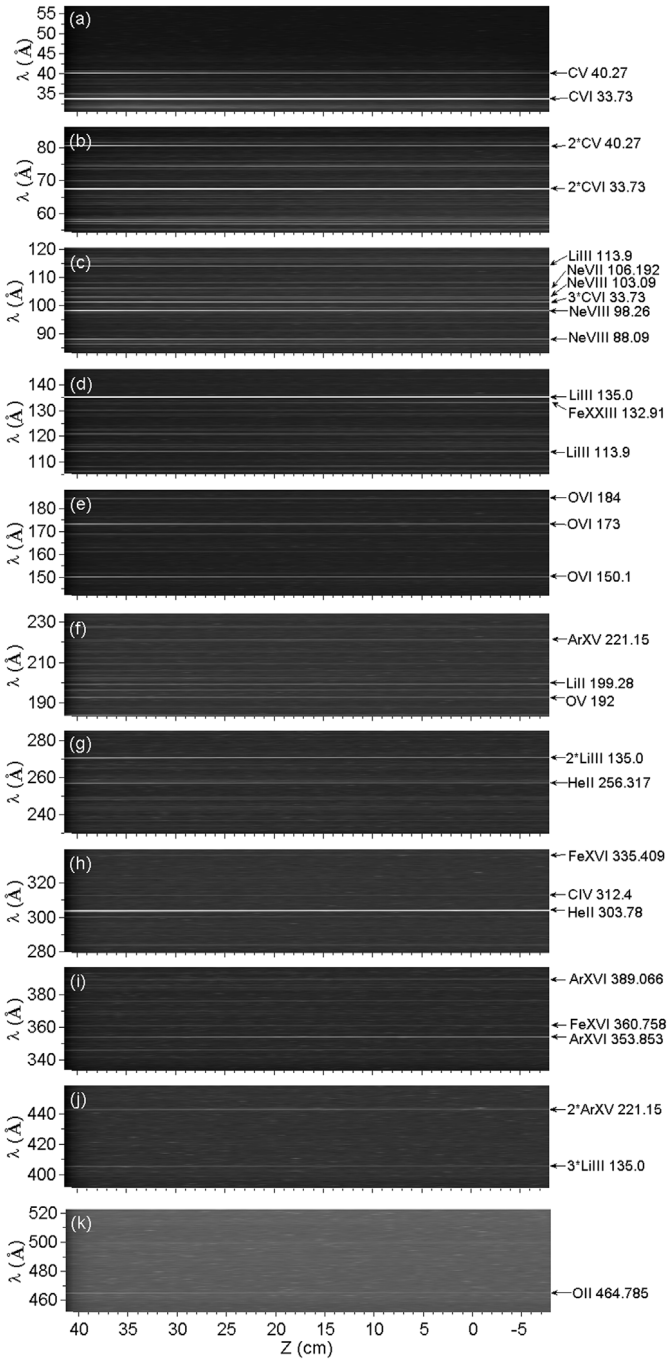

Fig. 6. Two-dimensional CCD images observed from Ohmic discharges; (a) 30.5–56.8 Å, (b) 54.3–86.1 Å, (c) 83.1–120.4 Å, (d) 105.2–146.0 Å, (e) 142.1–187.9 Å, (f) 183.3–233.9 Å, (g) 229.4–284.6 Å, (h) 279.5–338.9 Å, (i) 333.4–396.7 Å, (j) 391.0–458.1 Å and (k) 451.7–522.2 Å . The value of 'Z' denotes vertical position in plasma, and identified lines are denoted on the right hand side.

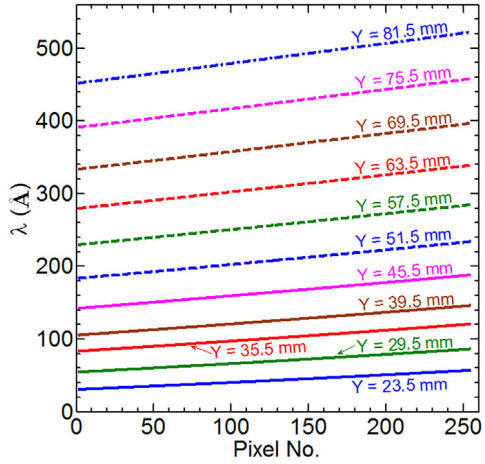

Fig. 7. Wavelength position on the short axis of CCD as a parameter of CCD positions, Y, on the focal plane shown in Fig. 1.

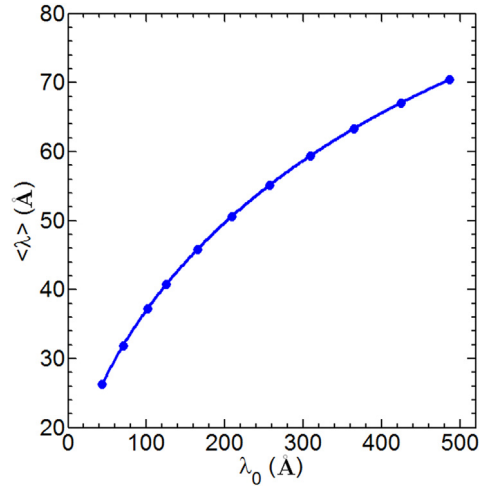

Fig. 8. Simultaneously observable wavelength interval, $\langle\lambda\rangle$, as function of central wavelength, λ_0, for different CCD positions shown in Fig. 7.

As illustrated in Fig. 2, the spectrometer is installed behind a long extension tube connected to a horizontal midplane port at toroidal port position of C (C port), which is mainly used for vacuum pumping system of EAST. The long distance of 8.835 m between the entrance slit and plasma center is required for ensuring a wide vertical observation range of 48.5 cm. The vertical range for spatial profile measurement is adjustable by pivoting the vertical angle of the spectrometer optical axis. The angle of declination of the spectrometer axis, θ_{EUV}, is usually fixed to $\theta_{EUV} = 1.4°$as shown in Fig. 2 to observe the vertical profile of impurity line emissions at the upper half plasma, i.e. $-8.5 \le Z \le 40$ cm ($-0.1 \le \rho \le 0.6$). The optical axis position is carefully adjusted at zeroth order light using a visible He–Ne laser directly attached to the spectrometer, as shown in the Fig. 3. In addition, the vertical position is exactly calibrated with a ROMER portable arm by inserting into the vacuum vessel before the experimental campaign.

The vertical observation range of the space-resolved EUV spectrometer (EUV_Long2) at $\theta_{EUV} = -1.4°$ is indicated in Fig. 4. The line of sight of the fast-response EUV spectrometers (EUV_Long and EUV_Short) is also plotted in Fig. 4. It is noted that the vertical observation range of the two fast-response EUV spectrometers is narrow, i.e. ~30 cm, because the long axis of the CCD is set horizontally along the wavelength dispersion. Since all EUV spectrometers are evacuated with a turbo-molecular pump, the vacuum pressure is always kept at the order of 10^{-5} Pa.

2.2. Wavelength calibration and spectral resolution

Before checking the performance of the space-resolved EUV spectrometer, wavelength positions on the CCD are calibrated using accurately determined wavelengths of well-known impurity spectra. For the purpose impurity spectra from the space-resolved EUV spectrometer are

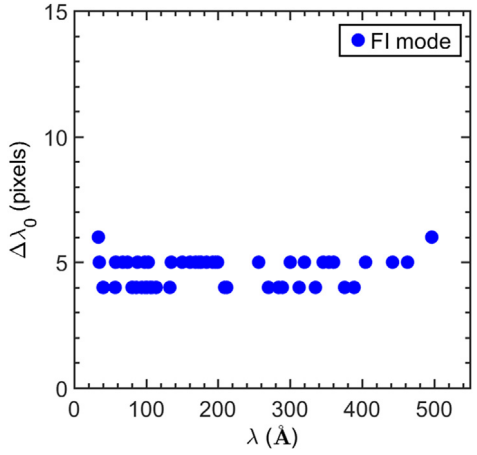

Fig. 9. Spectral resolution of space-resolved EUV spectrometer, $\Delta\lambda_0$, (full width at foot position of spectral line) as a function of wavelength. Several impurity lines, which are measured at full image (FI) mode in CCD operation, are used for checking.

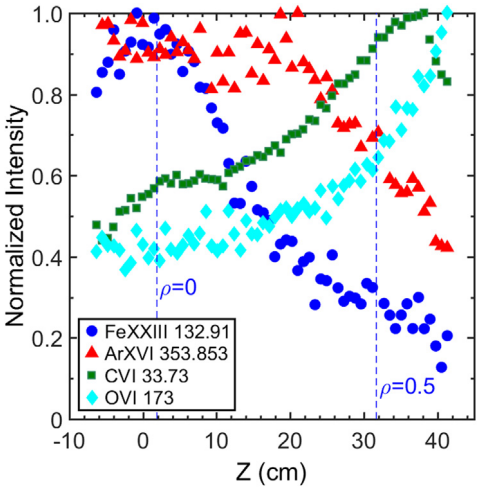

Fig. 10. Normalized vertical profiles of line intensity of Fe XXIII at 132.91 Å, Ar XVI at 353.853 Å, C VI at 33.73 Å and O VI at 173 Å in EAST Ohmic discharges. The vertical profile is disappeared at Z > 42 cm due to the limited observation range as shown in Fig. 2.

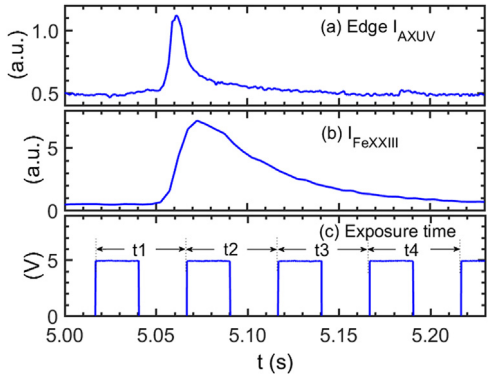

Fig. 11. Time evolutions of (a) edge radiation power (b) Fe XXIII intensity at 132.91 Å from fast-response EUV spectrometer (EUV_Long) and (c) CCD exposure time pulses (23.66 ms) during sudden increase in iron influx in RF heated discharges. Sampling time of CCD is set to 50 ms. The values of t1–t4 denote four successive CCD data sampling.

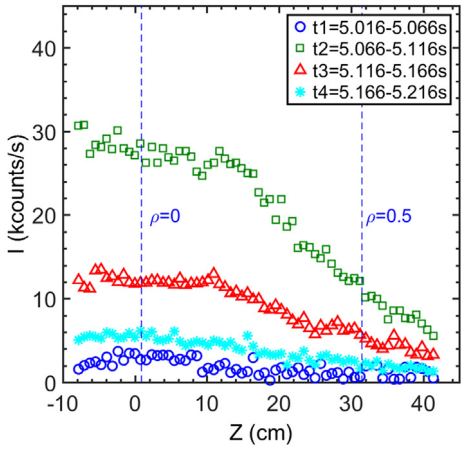

Fig. 12. Vertical profiles of Fe XXIII at 132.91 Å during sudden increase in iron influx shown in Fig. 11. Timings of t1–t4 are indicated in Fig. 11(c).

compared with those from the fast-response EUV spectrometer for which the wavelength position has been already calibrated.

Fig. 5(a)–(b) illustrate the EUV spectrum in the wavelength range of 20–500 Å measured by two fast-response EUV spectrometers in Ohmic discharges with upper single null tungsten divertor configuration. The central electron temperature in the Ohmic discharges is $T_{e0} \sim 1.0$ keV. The spectrum at 20–40 Å is measured with EUV_Short in a single discharge. The spectrum at 40–500 Å is a superposition of three spectra at different wavelength ranges measured with EUV_Long using three discharges. Line identifications of the spectrum show that dominant line emissions arise from hydrogen- and helium-like ions in intrinsically existing low-Z impurities such as He, Li, C, N and O. Since Ne line emissions appear around 100 Å and Ar line emissions also appear at wavelength range of 180–400 Å, those are tentatively observed as an aftereffect of the radiated divertor experiment with Ne and Ar seeding. The second order light, e.g., C VI 2 × 33.73 Å, Li III 2 × 135.0 Å and Ar XV 2 × 221.15 Å, are also used for the wavelength calibration.

Fig. 6(a)–(k) illustrate CCD images used for the wavelength calibration of EUV_Long2 which are taken with eleven Ohmic discharges. Since all line emissions observed in Fig. 6 locate in edge plasmas, almost constant intensity is recorded along the whole vertical range. It is noted here that the image brightness in Fig. 6 is different in each figure. A result of the wavelength calibration is shown in Fig. 7 as a function of pixel numbers at short axis of CCD. The parameter of Y denotes the CCD position on the focal plane shown in Fig. 1. In practice, the wavelength position has a non-linear relation to the pixel number of CCD. Almost all line emissions appearing in the EUV spectra from EUV_Long can be observed from EUV_Long2. It means the throughput of EUV_Long2 is sufficiently high. The signal intensity of line emissions is weaker at longer wavelengths, reflecting a reduction of the grating reflectivity. It is clear from the figure that a simultaneously observable wavelength range, $\langle\lambda\rangle$, changes according to the CCD position. The value of $\langle\lambda\rangle$ determined from the CCD short-axis length of 6.6 mm is shown in Fig. 8. It varies against the wavelength in the range $\langle\lambda\rangle$ = 26–70 Å, e.g. $\langle\lambda\rangle$ = 29 Å (38 ≤ λ ≤ 67 Å) at λ_0 = 50 Å (Y = 25.5 mm) and $\langle\lambda\rangle$ = 68 Å (420 ≤ λ ≤ 488 Å) at λ_0 = 450 Å (Y = 78.5 mm). Therefore, eleven discharges are necessary for measuring the whole wavelength range of 30–520 Å, as shown in Fig. 6.

The spectral resolution is also examined at full image mode operation of the CCD. The result is plotted in Fig. 9. An excellent spectral resolution of $\Delta\lambda_0$ = 4–5 pixels is obtained in a wide wavelength range of 40–480 Å. Here, the value of $\Delta\lambda_0$ is defined as the full width at foot position of a spectral line. Then, the spectral resolution at the full width at half maximum (FWHM) is nearly 0.22 Å at 100 Å.

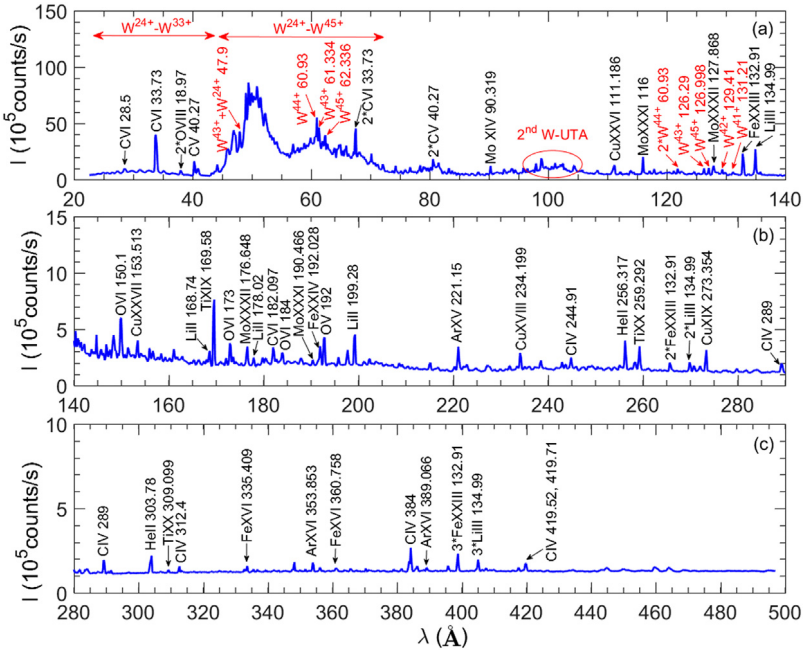

Fig. 13. Typical EUV spectra observed with EUV_Long from EAST H-mode discharges in wavelength ranges of (a) 20–140 Å, (b) 140–290 Å and (c) 280–500 Å. The spectrum at 20–500 Å measured with EUV_Long using three discharges are superposed by three spectra at different wavelength ranges.

2.3. Radial profiles of impurity line emissions

Vertical intensity profiles of Fe XXIII at 132.91 Å (ionization energy of Fe^{22+} ion, E_i (Fe^{22+}) = 1950 eV), Ar XVI at 353.853 Å (E_i (Ar^{15+}) = 918 eV), C VI at 33.73 Å (E_i (C^{5+}) = 490 eV) and O VI at 173 Å (E_i (O^{5+}) = 138 eV) observed in Ohmic discharges are plotted in Fig. 10. It is clearly seen that the peak position in the radial profile moves inside with the ionization energy. The line intensity in Fig. 10 is obtained by integrating the signal counts within the spectral resolution of $\Delta\lambda_0$ shown in Fig. 9. The background count is subtracted using a smaller count at the left or right foot position of the spectral profile. One can see in the figure that the radial profile disappears at Z > 42 cm. This is due to the limited observation range as shown in Fig. 2. The upper observation chord is limited by an edge of the diagnostic port. In the present arrangement, therefore, it is difficult to measure the full vertical profile at the upper-half of plasmas, including the vicinity of the separatrix. However, if line emission is located in the plasma center within $\rho = 0.6$, e.g. highly ionized ions from heavy impurities as described later, it is possible to observe an entire radial profile even in the present arrangement.

When the CCD is operated in full image (FI) mode with 1024 × 255 pixels, a long sampling time is necessary for acquiring the data, e.g. ~800 ms/frame. Then, the sub-image mode is used to reduce the sampling time and to ensure a sufficient temporal resolution. When the signal binning is made every 8 or 16 pixels along the long axis of the CCD, the sampling time can be reduced to 200 ms, resulting in a spatial resolution of 2.1 cm or 2.5 cm, respectively. If the signal binning is also made for the short axis of the CCD, the sampling time can be much reduced, e.g. 50 ms/frame at 5 pixel binning. During the experiment, the CCD is externally triggered by a 10 ms width TTL pulse from the EAST control system delivered a minute before the discharge start.

The radial profile measurement with high temporal resolution is attempted at 50 ms/frame. A sudden impurity buildup event occurred in RF discharges as shown in Fig. 11, which is caused by an unexpected arcing from an antenna made of stainless steel. The temporal evolution of the edge radiation measured by the AXUV system in Fig. 11(a) shows the sudden increase in the iron influx during 20 ms. The temporal behavior of Fe XXIII measured at 132.91 Å with EUV_Long in Fig. 11(b) shows a rapid rise coinciding with the edge radiation and a gradual decay of ~150 ms which indicates a long duration of Fe^{22+} ions in the plasma. The CCD exposure time with 23.66 ms pulse width for EUV_Long2 is indicated in Fig. 11(c) at every 50 ms. Time-developed Fe XXIII radial profiles during the sudden impurity buildup event are plotted in Fig. 12 for four successive frames. Almost entire radial profiles are sufficiently observed within the observation range at $\rho \leq 0.6$. The temporal intensity behavior of Fe XXIII from EUV_Long2 in Fig. 12 shows a good agreement with that from EUV_Long in Fig. 11(b). Both EUV_Long and EUV_Long2 spectrometers indicate that the Fe XXIII intensity at t2 timing is 6 times higher than that at t4 timing. The result demonstrates the space-resolved EUV spectrometer developed here works well to study impurity transport in EAST.

3. Radial profiles of tungsten spectra in H-mode discharges

Fig. 13 illustrates typical EUV spectra from EUV_Long observed in RF heated H-mode discharges of EAST with heating power of P_{LHW} = 2.0–2.5, P_{ICRH} = 1.2–1.8 and P_{ECRH} = 0.3 MW. The discharges are carried out at line-averaged electron density of $n_e = 3.5 \times 10^{13}$ cm^{-3} and central electron temperature of T_{e0} = 3.0–3.5 keV. In the spectra the pseudo-continuum called unresolved transition array (UTA) clearly appears at 40–75 Å as a typical indication of the tungsten spectrum. Line emissions from highly ionized ions from high-Z impurities including tungsten are also observed in the spectra, e.g., Ti XIX-Ti XX, Cu XXVI-Cu XXVII, Mo XXXI-Mo XXXII and W XLII-W XLVI. The CCD images from EUV_Long2 are shown in Fig. 14. Those are also observed from RF heated H-mode discharges similar to Fig. 13 in which the tungsten line emissions are sufficiently strong. Identified line emissions are denoted on the right hand of the CCD image. Many spectral lines are closely emitted below 200 Å. Contrary to this, the number of lines is relatively small above 200 Å. The line emissions identified from EUV_Long2 are almost identical to the result from EUV_Long in Fig. 13. It means that EUV_Long2 has sufficient spectral resolution for the tungsten diagnostics in EAST.

The W-UTA (5f-4d, 5p-4d, 6g-4f and 5g-4f transitions) composed of W^{24+}–W^{33+} ions appearing in the wavelength range of 20–40 Å is very weak, while the W-UTA (4f-4d, 4d-4p and 5d-4f transitions) composed of W^{24+}–W^{45+} appearing in the wavelength range of 45–70

Å is quite strong. The second order of the W-UTA near 50 Å is also observed near 100 Å. Although isolated line emissions from highly ionized tungsten ions, e.g., W^{41+}–W^{45+}, can be seen at 120–140 Å, the intensities are very weak. Then, the tungsten spectrum extended at 45–135 Å is replotted in Fig. 15(a)–(c). As seen in Fig. 15, many tungsten line emissions exist in the wavelength range of 45–135 Å. Detailed identifications are made for all the tungsten line emissions. In order to make accurate identification of tungsten line emissions, radial profiles of the tungsten line are extremely important as described in a previous report [20].

Vertical profiles of tungsten line emissions are analyzed from Fig. 14. The result is plotted in Fig. 16(a)–(c). Fig. 16(a) shows the vertical profile of three line emissions from highly ionized tungsten ions existing in the W-UTA wavelength range, i.e. W^{43+} ($4s^24p\ ^2P_{2/1} - 4s4p^2\ ^2D_{3/2}$) at 61.334 Å, W^{44+} ($4s^2\ ^1S_0 - 4s4p\ (1/2,3/2)_1$) at 60.93 Å and W^{45+} ($4s\ ^2S_{1/2} - 4p\ ^2P_{3/2}$) at 62.336 Å. When the vertical profile of W^{43+}–W^{45+} ions is referred to the identification of tungsten line spectra, the ionization stage in other tungsten lines can be easily estimated. For example, the vertical profile of the tungsten line at 47.15 Å shown in Fig. 15(a) is entirely overlapped with that of the W^{43+} at 61.334 Å in Fig. 16(a). Then, we notice that the line at 47.15 Å arises from the W^{43+} ion. The same method is applied to the analysis of W-UTA near 50 Å. Vertical profiles at three wavelength intervals indicated by shaded areas at 48.8–50.0 Å in Fig. 15(a) are plotted in Fig. 16(b). When we compare the peak position among three radial profiles, each peak locates in different radial positions. Then, we can easily identify that three wavelength intervals of 48.81–49.02 Å, 49.24–49.57 Å and 49.79–50.01 Å arise from W^{26+}, W^{27+} and W^{29+}, respectively [20]. The ionization stage of other tungsten line emissions at the W-UTA in Fig. 15(a) is also determined through the analysis of vertical profiles observed from EUV_Long2.

Vertical profiles of isolated line emissions are plotted in Fig. 16(c) and (d). Fig. 16(c) shows vertical profiles of W^{42+} ($4s^24p^2\ ^3P_0 - 4s^24p^2\ ^1D_2$) at 129.41 Å, W^{43+} ($4s^24p\ ^2P_{1/2} - 4s^24p\ ^2P_{3/2}$) at 126.29 Å and W^{45+} ($4s\ ^2S_{1/2} - 4p\ ^2P_{1/2}$) at 126.998 Å. We notice that the radial profiles are more peaked compared to those in Fig. 16(a) due to the relatively low electron temperature of $T_{e0} = 2.9$ keV. Fig. 16(d) shows vertical profiles of other heavy impurities, i.e. Cu XXVI ($2s^2\ ^1S_0 - 2s2p\ ^1P_1$, $E_i = 2479$ eV) at 111.186 Å, Mo XXXI ($3s^2\ ^1S_0 - 3s3p\ ^1P_1$, $E_i = 1730$ eV) at 116.0 Å and Fe XXIII ($2s^2\ ^1S_0 - 2s2p\ ^1P_1$, $E_i = 1950$ eV) at 132.9 Å. The line emission from Fe XXIII at 132.91 Å is totally overlapped with W^{44+} ($4s^2\ ^1S_0 - 4s4p\ P_{1/2}$, $E_i = 2355$ eV) at 132.88 Å. On the other hand, the space-resolved EUV spectrometer system can supply information on the top-to-bottom profile symmetry/asymmetry, while the vertical range is limited to a narrow region of $-10 \le Z \le 10$ cm in the present geometry. When we compare the radial profile between lower and upper regions near the plasma center, i.e. $-10 \le Z \le 0$ cm and $0 \le Z \le 10$ cm, it may suggest an asymmetric profile. Further experiments are necessary to confirm the truth by changing the vertical observation range.

4. Preliminary analysis of tungsten ion density profile

The chord-integrated intensity of tungsten line at vertical position of Z can be calculated by integrating the local emissivity along the line of sight of EUV_Long2 with the following equation of

$$I^{W^{q+}}(Z) = \int \varepsilon^{W^{q+}}(Z,l)\,dl = \int n^{W^{q+}}(Z,l)\,PEC^{W^{q+}}(Z,l)\,n_e(Z,l)\,dl, \qquad (2)$$

where $I^{W^{q+}}$ and $\varepsilon^{W^{q+}}$ mean the intensity and local emissivity of line emission from tungsten ions with ionization stage of q, and $n^{W^{q+}}$ and $PEC^{W^{q+}}$ mean the density of W^{q+} ions and photon emissivity coefficient of the line emission, respectively. The tungsten ion density profile is then analyzed from the vertical intensity profile. Firstly, the spectral intensity measured with EUV_Long2 has to be absolutely calibrated, and then the local emissivity profile of tungsten lines can be reconstructed from the vertical intensity profile based on Abel inversion calculation. Finally, the density profile of tungsten ions is obtained with measured T_e and n_e profiles and the PEC data.

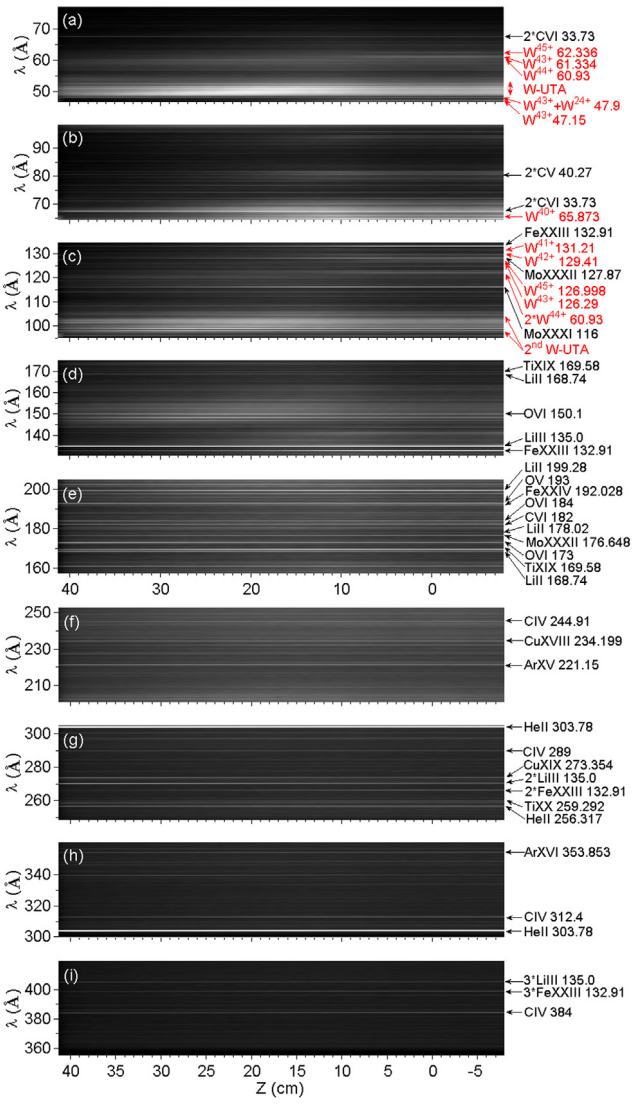

Fig. 14. Typical two-dimensional CCD images observed from H-mode discharges (T_{e0} = 2.9–4.0 keV and $n_e \sim 3.5 \times 10^{19}$ m^{-3}); (a) 46.6–76.9 Å, (b) 64.4–98.3 Å, (c) 95.1–134.4 Å, (d) 130.5–174.9 Å, (e) 157.2–204.8 Å, (f) 200.3–252.6 Å, (g) 248.0–304.8 Å, (h) 299.1–360.0 Å and (i) 354.6–419.4 Å. The value of 'Z' denotes vertical position in plasma, and identified lines are denoted on the right hand side.

The absolute calibration for the space-resolved EUV spectrometer has been excellently carried out at high-density discharges with $n_{e0} = 2.2 \times 10^{14}$ cm^{-3} in LHD [29,30]. The EUV bremsstrahlung continuum intensity is accurately calculated from measured visible bremsstrahlung intensity profile with T_e profile. The calibration factor can be then obtained by comparing the EUV bremsstrahlung intensity profile between measurement and calculation. Since the operational density limit of EAST is relatively low, e.g. $n_{e0} = 5.5 \times 10^{13}$ cm^{-3}, the EUV bremsstrahlung intensity from EUV_Long2 is weak due to the relatively low throughput compared to EUV_Long. In addition, the visible bremsstrahlung measurement in EAST has no sufficient profile data. Then, the calibration of EUV_Long2 is only carried out at shorter wavelength range where the EUV bremsstrahlung emission is strong, referring the calibration data of EUV_Long in which the spectral intensity has been already calibrated [36], e.g. 4×10^9 phs cm^{-2} s^{-1}/(counts s^{-1}) at 62 Å and 8.5×10^9 phs cm^{-2} s^{-1}/(counts s^{-1}) at 130 Å. Since the

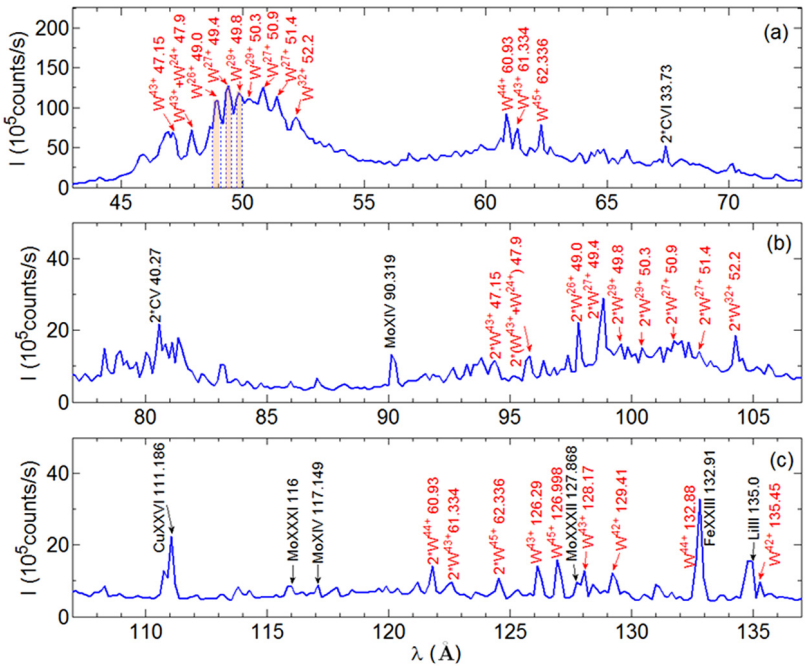

Fig. 15. Tungsten spectra in different wavelength ranges of (a) 43–73 Å, (b) 77–107 Å and (c) 107–137 Å in RF heated H-mode discharges (T_{e0} = 3.3 keV, #67682). Three shaded areas at 48.8–50.0 Å in (a) indicate the wavelength interval in W-UTA used for vertical profile measurement shown in Fig. 16(b).

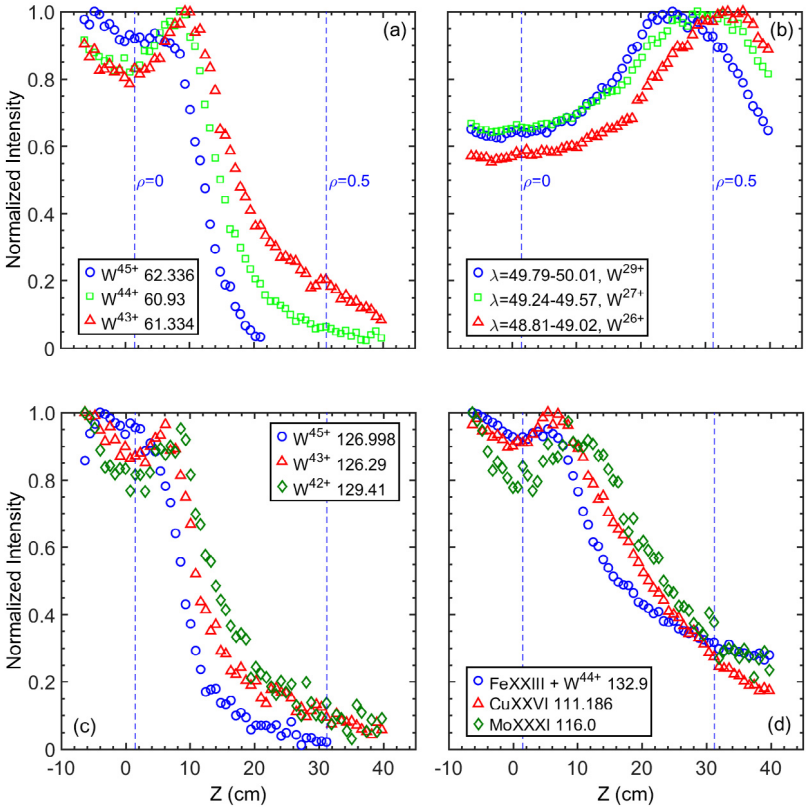

Fig. 16. Vertical intensity profile of (a) W^{45+} (62.336 Å), W^{44+} (60.93 Å) and W^{43+} (61.334 Å) in W-UTA, (b) W^{26+}–W^{29+}, (c) W^{45+} (126.998 Å), W^{43+} (126.29 Å) and W^{42+} (129.41 Å) and (d) Fe XXIII blended with W^{44+} (132.9 Å), Cu XXVI (111.186 Å) and Mo XXXI (116.0 Å) . The radial locations of ρ = 0 and 0.5 are indicated with vertical dashed lines. Data are taken from H-mode discharges with T_{e0} = 3.3 keV ((a) and (b)) and 2.9 keV ((c) and (d)).

same grating and CCD as LHD is being used in EAST, we assume the wavelength dependence of the calibration factor is identical between EAST and LHD. Thus, the vertical intensity profiles are obtained for tungsten line emissions as shown in Fig. 17(a) and (c). Fig. 17(a) shows the intensity profiles of W^{45+} at 62.336 Å, W^{44+} at 60.93 Å and W^{43+} at 61.334 Å from H-mode plasmas with T_{e0} = 3.3 keV and Fig. 17(c)

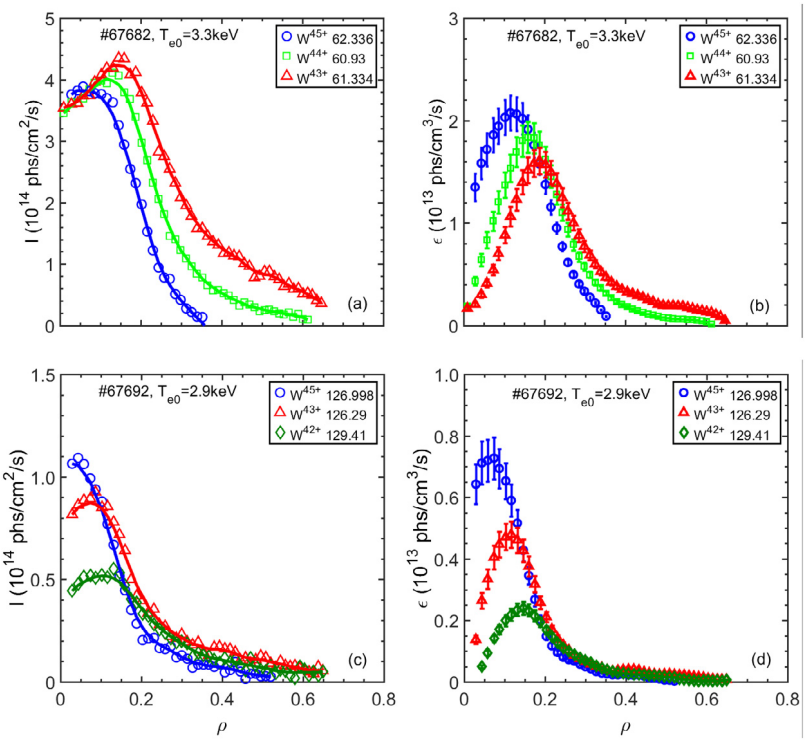

Fig. 17. Radial profiles of (a) chord-integrated line intensity and (b) local emissivity of W^{45+} (62.336 Å), W^{44+} (60.93 Å) and W^{43+} (61.334 Å) and (c) chord-integrated line intensity and (d) local emissivity of W^{45+} (126.998 Å), W^{43+} (126.29 Å) and W^{42+} (129.41 Å). Data are taken from H-mode discharges with T_{e0} = 3.3 keV ((a) and (b)) and 2.9 keV ((c) and (d)).

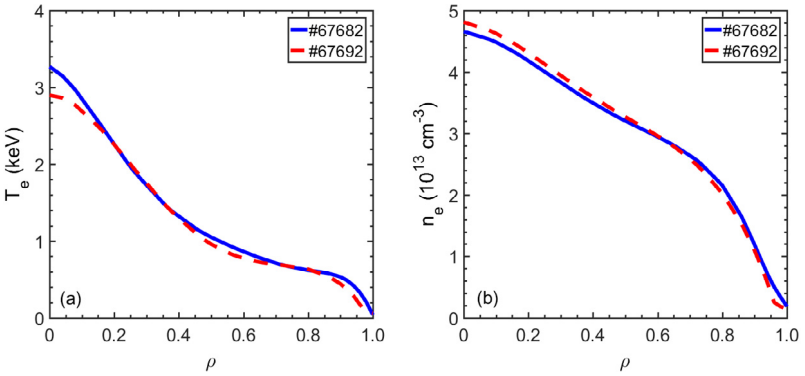

Fig. 18. Radial profiles of (a) electron temperature and (b) electron density.

shows W^{45+} at 126.998 Å, W^{43+} at 126.29 Å and W^{42+} at 129.41 Å from H-mode plasmas with T_{e0} = 2.9 keV.

The local emissivity profiles of tungsten line emissions reconstructed from Fig. 17(a) and (c) are plotted in Fig. 17(b) and (d), respectively. The local emissivity of tungsten line emissions at the peak position increases with the ionization stage. In particular, it is noticeable in the low-temperature discharge case of Fig. 17(d). It is not clear at the moment whether the emission increase in higher ionization stages indicates the tungsten accumulation in H-mode discharges. Impurity transport simulation is necessary for further study.

In order to evaluate the tungsten ion density, PEC data from open-ADAS (arf40_ic series) is used in the present study. Based on the T_e and n_e profiles measured during H-mode phase shown in Fig. 18(a) and (b), the ion density profiles of W^{43+} and W^{45+} are obtained. The result is plotted in Fig. 19. It is found that the density of W^{43+}–W^{45+} ions is distributed in range of 2–6 × 10^8 cm^{-3} in H-mode discharges which we have analyzed in the present study.

5. Summary

A space-resolved spectrometer working at 30–520 Å is newly developed to measure the tungsten emission profiles. Good spectral resolution of $\Delta\lambda_0$ = 4–5 pixels at 100 Å (0.22 Å at FWHM), sufficient temporal resolution of 50 ms and high spatial resolution of 2.5 cm are obtained simultaneously. As a result, excellent vertical profiles from several impurities are successfully observed from Ohmic and H-mode plasmas in the EAST tokamak. Vertical profiles of tungsten emissions from W^{42+} – W^{45+} ions are also measured at 45–70 Å and 120–140 Å in high-temperature discharges at $T_e \geq 2.5$ keV. The density profile of such highly ionized tungsten ions is evaluated from the vertical profile. The preliminary analysis shows that the densities of W^{43+}–W^{45+} ions range in 2–6 × 10^8 cm^{-3} in H-mode plasmas.

The tungsten transport study is crucially important in long pulse H-mode operations of EAST with tungsten divertor. It is then concluded that the radial profile measurement of impurity line emissions with

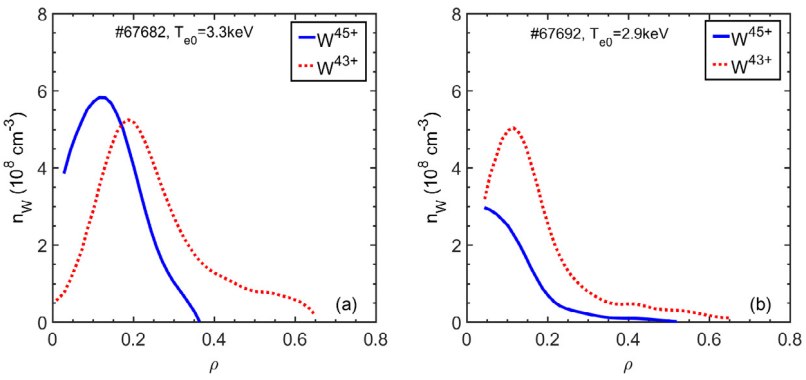

Fig. 19. Calculated radial profiles of W^{45+} and W^{43+} ion density in steady-state H-mode phase in (a) T_{e0} = 3.3 keV and (b) T_{e0} = 2.9 keV. PEC from ADAS database is applied in the calculation.

high temporal and spatial resolutions based on the present space-resolve spectrometer enables the impurity transport study in H-mode discharges of EAST.

Acknowledgments

This work was supported by the National Natural Science Foundation of China (Grant Nos. 11575244, 11775269), the National Magnetic Confinement Fusion Science Program of China (Grant Nos. 2014GB124006, 2015GB101000) and National Key Research and Development Program of China (No. 2017YFE0301300).

References

[1] V. Philipps, Tungsten as material for plasma-facing components in fusion devices, J. Nucl. Mater. 415 (2011) S2–S9.
[2] Y. Wan, J. Li, Y. Liu, et al., Overview of the present progress and activities on the CFETR, Nucl. Fusion 57 (2017) 102009.
[3] R. Neu, M. Balden, V. Bobkov, et al., Plasma wall interaction and its implication in an all tungsten divertor tokamak, Plasma Phys. Control. Fusion 49 (2007) B59.
[4] J. Bucalossi, M. Missirlian, P. Moreau, et al., The WEST project: Testing ITER divertor high heat flux component technology in a steady state tokamak environment, Fusion Eng. Des. 89 (2014) 907–912.
[5] G.F. Matthews, M. Beurskens, S. Brezinsek, et al., JET ITER-like wall-overview and experimental programme, Phys. Scr. T145 (2011) 014001.
[6] D. Yao, G. Luo, S. Du, et al., Overview of the EAST in-vessel components upgrade, Fusion Eng. Des. 98–99 (2015) 1692.
[7] K. Holtrop, D. Buchenauer, C. Chrobak, et al., The design and use of tungsten coated TZM molybdenum tile inserts in the DIII-D Tokamak divertor, Fusion Sci. Technol. 72 (2017) 1–6.
[8] T. Nakano, Tungsten transport and accumulation in JT-60U, J. Nucl. Mater. 415 (2011) S327–S333.
[9] M.B. Chowdhuri, S. Morita, M. Goto, et al., Line analysis of EUV spectra from molybdenum and tungsten injected with impurity pellets in LHD, Plasma Fusion Res. 2 (2007) S1060.
[10] X. Huang, S. Morita, T. Oishi, et al., Coaxial pellets for metallic impurity injection on the large helical device, Rev. Sci. Instrum. 85 (2014) 11E818.
[11] K. Zhang, Z.Y. Cui, P. Sun, et al., Investigation of impurity transport using laser blow-off technique in the HL-2A Ohmic and ECRH plasmas, Chin. Phys. B 25 (2016) 065202.
[12] A. Loarte, M.L. Reinke, A.R. Polevoi, et al., Tungsten impurity transport experiments in Alcator C-Mod to address high priority research and development for ITER, Phys. Plasma 22 (2015) B207.
[13] J. Clementson, P. Beiersdorfer, A.L. Roquemore, et al., Experimental setup for tungsten transport studies at the NSTX tokamak, Rev. Sci. Instrum. 81 (2010) 10E326.
[14] S. Morita, C. Dong, M. Goto, et al., A study of tungsten spectra using large helical device and compact electron beam ion trap in NIFS, AIP Conf. Proc. 1545 (2013) 143.
[15] H. Mao, F. Ding, G. Luo, et al., A multichannel visible spectroscopy system for the ITER-like W divertor on EAST, Rev. Sci. Instrum. 88 (2017) 043502.
[16] T. Oishi, S. Morita, X. Huang, et al., Observation of W IV–W VII line emissions in wavelength range of 495–1475 Å in the large helical device, Phys. Scr. 91 (2016) 025602.
[17] K. Asmussen, K.B. Fournier, J.M. Laming, et al., Spectroscopic investigations of tungsten in the EUV region and the determination of its concentration in tokamaks, Nucl. Fusion 38 (1998) 967.
[18] T. Pütterich, R. Neu, R. Dux, et al., Modelling of measured tungsten spectra from ASDEX, Upgrade and predictions for ITER, Plasma Phys. Control. Fusion 50 (2008) 085016.
[19] L. Zhang, S. Morita, Z. Xu, et al., Suppression of tungsten accumulation during ELMy H-mode by lower hybrid wave heating in the EAST tokamak, Nucl. Mater. Energy 12 (2017) 774–778.
[20] Y. Liu, S. Morita, X. Huang, et al., Component investigation of ionization stages on tungsten unresolved transition array spectra for plasma diagnostics based on space-resolved extreme-ultra violet spectroscopy in large helical device, J. Appl. Phys. 122 (2017) 233301.
[21] Y. Liu, S. Morita, T. Oishi, et al., Observation of tungsten line emissions in wavelength range of 10-500Å in Large Helical Device, Plasma Fusion Res. 13 (2018) 3402020.
[22] T. Nakano, A.E. Shumack, C.F. Maggi, et al., Determination of tungsten and molybdenum concentrations from an x-ray range spectrum in JET with the ITER-like wall configuration, J. Phys. B: At. Mol. Opt. Phys. 48 (2015) 144023.
[23] M.B. Chowdhuri, S. Morita, M. Goto, Characteristics of an absolutely calibrated flat-field extreme ultraviolet spectrometer in the 10–130 Å range for fusion plasma diagnostics, Appl. Opt. 47 (2008) 135.
[24] M.A. Janzer, Tungsten transport in the plasma edge at ASDEX Upgrade (Ph.D. thesis), 2015.
[25] J.K. Lepson, P. Beiersdorfer, J. Clementson, et al., EUV spectroscopy on NSTX, J. Phys. B: At. Mol. Opt. Phys. 43 (2010) 144018.
[26] C. Dong, S. Morita, M. Goto, et al., Space-resolved extreme ultraviolet spectrometer for impurity emission profile measurement in Large Helical Device, Rev. Sci. Instrum. 81 (2010) 033107.
[27] X. Huang, S. Morita, T. Oishi, et al., Space-resolved extreme ultraviolet spectroscopy free of high-energy neutral particle noise in wavelength range of 10–130 Å on the large helical device, Rev. Sci. Instrum. 85 (2014) 043511.
[28] X. Huang, S. Morita, T. Oishi, et al., Formation of impurity transport barrier in LHD plasmas with hollow density profile, Nucl. Fusion 57 (2017) 086031.
[29] C. Dong, S. Morita, M. Goto, et al., Absolute intensity calibration of flat-field space-resolved extreme ultraviolet spectrometer using radial profiles of visible and extreme ultraviolet bremsstrahlung continuum emitted from high-density plasmas in Large Helical Device, Rev. Sci. Instrum. 82 (2011) 113102.
[30] C. Dong, S. Morita, M. Goto, et al., Extension of wavelength range in absolute intensity calibration of space-resolved EUV spectrometer for LHD diagnostics, Plasma Fusion Res. 7 (2012) 2402139.
[31] Z. Cui, H. Zhou, S. Morita, et al., Space-resolved VUV and EUV spectrometers in HL-2A, Plasma Sci. Technol. 15 (2013) 110.
[32] Y. Shen, X. Du, W. Zhang, et al., Space-resolved extreme ultraviolet spectrometer system for impurity behavior research on experimental advanced superconducting Tokamak, Nucl. Instrum. Methods Phys. Res. 700 (2013) 86–90.
[33] Y. Shen, B. Lu, X. Du, et al., Spatially-resolved flat-field soft X-ray spectrometer on experimental advanced superconducting tokamak, Fusion Eng. Des. 88 (2013) 3072–3077.
[34] E. Wang, S. Morita, M. Goto, et al., Two-dimensional measurement of edge impurity emissions using space-resolved extreme ultraviolet spectrometer in Large Helical Device, Rev. Sci. Instrum. 83 (2012) 043503.
[35] H. Zhang, S. Morita, T. Oishi, et al., Performance improvement of two-dimensional EUV spectroscopy based on high-frame-rate CCD and signal normalization method in Large Helical Device, J. Jpn. Appl. Phys. 54 (2015) 086101.
[36] L. Zhang, S. Morita, Z. Xu, et al., A fast-time-response extreme ultraviolet spectrometer for measurement of impurity line emissions in the Experimental Advanced Superconducting Tokamak, Rev. Sci. Instrum. 86 (2015) 123509.